Giant Photonic Spin Hall Effect by Anisotropic Band in Photonic Crystal Slabs

Rongfeng Zhang, Hongwei Yang, Huifeng Chen, Wenguo Zhu [ID], Huadan Zheng, Jianhui Yu, Yongchun Zhong, and Zhe Chen

Abstract—When a paraxial light beam is reflected from/transmitted through an optical element with rotation symmetry, a tiny small incident angle can arise wave-vector-varying Pancharatnam-Berry (PB) phases, resulting in high-performance photonic spin Hall effect (PSHE). Differently, here we investigate the PSHE in photonic crystal slabs of square lattices constructed with air holes, and demonstrate that the C_{4v} symmetry of the slabs enables giant PSHE in both isotropic and anisotropic band structures with a small incident angle. The guided-mode resonances of the subwavelength-thickness slab enhance the PSHE, allowing the spin separation to exceed the incident beam waist. Via changing the incident angle, wavelength and even the beam waist, the spin separation can be adjusted in a wide range, which makes our proposal more flexible in manipulation of spin photons.

Index Terms—Photonic spin hall effect, photonic crystal slabs, spin separation, pancharatnam-berry phases.

I. INTRODUCTION

PHOTONIC Spin Hall Effect (PSHE) associated with the geometric phase is caused by spin-orbit interactions when a paraxial light beam projected onto an oblique plane is reflected or transmitted at an interface [1], [2], [3]. Typically, PSHE causes photons with opposite spin components to split spatially into left-handed circularly polarized (LCP) and right-handed circularly polarized (RCP) light [4], [5], [6], [7]. In other words, featured by spin-dependent displacements, PSHE introduces additional spin degrees of freedom for the flexible manipulation of light, and has attracted much attention in various realms, including optical sensing, precision metrology and nanophotonic devices [8], [9], [10], [11]. However, the weak spin-orbit

interactions result in a generally weak PSHE [12], [13], [14], [15], [16], [17]. Although various methods have been demonstrated to enhance the PSHE, the enhancements sacrifice the energy efficient. Recently, a novel PSHE was proposed based on the wave-vector-varying Pancharatnam-Berry (PB) phases, allowing us to address the contradiction between spin separation and energy efficiency in the conventional PSHE [18]. The wave-vector-varying PB phases arise naturally when a paraxial light beam is reflected from or transmitted through an optical element with rotation symmetry with a tiny small incident angle. With a uniaxial yttrium vanadate crystal, the opposite-spin photons of transmitting beam can be completely separated with a spin separation of 2.2 times the incident beam waist with a high energy efficiency of ~70% [19]. However, to form the rotation symmetric system, the optical axis of the uniaxial crystal is perpendicular to its input and output interfaces. The needed crystal length is up to 10 mm, which hinders the development of integrated spin-photonic devices.

Here, we investigate the PSHE in subwavelength-thickness photonic crystal (PhC) slabs of square lattices with air holes. Consisting of a periodic modulation of the refractive index at the wavelength scale, the PhC slabs can be used to realize many novel optical applications including filters [20], [21], [22], [23], [24], [25], [26], [27], optical vortex generation [28], structural color generation [23], and polarization tailoring [29]. The PhC slabs support both isotropic and anisotropic band structures [30]. We demonstrate here that giant PSHE from wave-vector-varying PB phases can be obtained in both isotropic and anisotropic band structures.

II. THEORY

Fig. 1 gives the structure of the proposed PhC slab. The PhC slab is a free-standing silicon nitride (Si_3N_4, refractive index 2.02) with periodic circular holes, the unit cell of which is shown in the inset of Fig. 1(a). The period of the lattice $a = 380$ nm, the thickness $t = 120$ nm, and the radius of the air hole $r = 140$ nm. The transmission spectra for s-plane wave are calculated with the finite element method (COMSOL Multiphysics 5.6) and shown in Fig. 1(b), where the white chain lines denote the four lowest TE-like bands along the Γ-X direction, while the magenta chain lines represent the TM-like bands. The transmission dip regions are overlapped well with the lines of lowest three bands. The complex transmission dips around 460 nm may be caused by the interaction of TE-like Band 4 and the TM-like bands. The four TE-like bands are above the light line, allowing them to
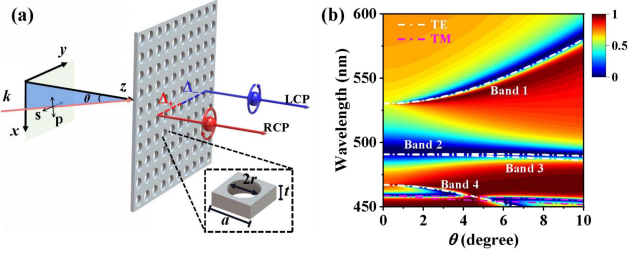
Fig. 1. (a) Schematic view of the proposed spin-splitting approach. The inset shows the schematic of the lattice. (b) Transmission spectra for s-plane wave incidence. And the white chain lines denote the four lowest TE-like bands along the Γ-X direction, while the magenta chain lines represent the TM-like bands.
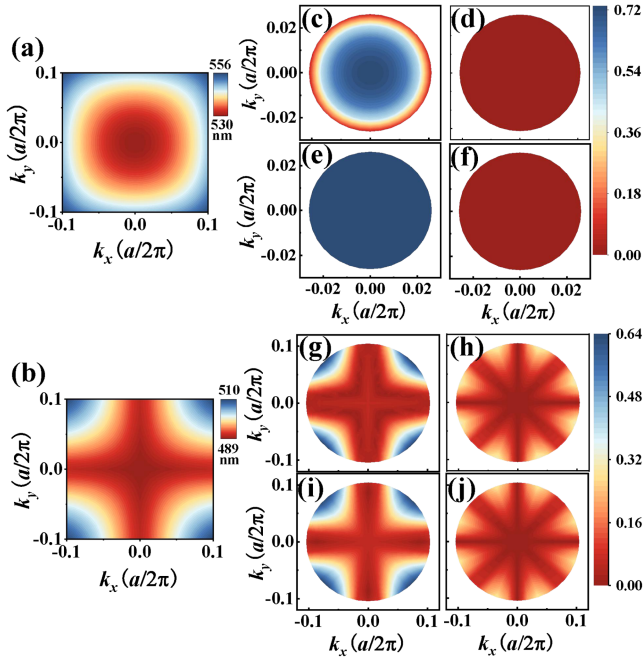

Fig. 2. (a), (b) Constant frequency contours of band 1 (a) and band 2 (b). (c)–(j) Contour plots of Fresnel transmission coefficients $|t_{ss}|$ (c), (g), $|t_{ps}|$ (d), (h), $|t_{pp}|$ (e), (i), and $|t_{sp}|$ (f), (j) as functions of k_x and k_y at 532 nm (c)–(f) and 493 nm (g)–(j) Wavelengths, respectively.

be coupled to by free-space illumination. Thus at these bands, guided-mode resonances occur. Especially, the Γ point at 530.6 nm is bound states in the continuum (BIC), with infinite life times and ideally Dirac transmission dip. On contrast, the transmission dips around 495 nm are wide, since Band 2 and 3 are very close to each other.

Fig. 2(a), (b) give a deep insight on the band structures near $\lambda = 532$ nm and 493 nm. Near $\lambda = 532$ nm, the band structure is in rotation symmetric, while which is in four-fold rotational symmetry for $\lambda = 493$ nm. The band structure makes influence to the transmission coefficients, as shown in Fig. 2(c)–(j), where the coefficients functions of transverse wavevector (k_x, k_y) are shown. At $\lambda = 532$ nm, coefficients $|t_{ss}|$ and $|t_{pp}|$ are rotationally symmetric, and $|t_{ps}|$ and $|t_{sp}|$ vanish identically. Thus, s and p polarizations are decoupled. At $\lambda = 493$ nm, however, the $|t_{ps}|$ and $|t_{sp}|$ are nonzero, except for at the lines of $k_x = 0$ and $k_y = 0$. The coupling of s and p polarizations is because the Band 2 and 3 are close to each other very much, they will be excited

simultaneously when the obliquely incident plane waves are not along a high symmetry plane.

In the following, we focus our attention on the PSHE of the transmitted beam from the PhC slab. The PhC slab can be considered as modulator in the momentum space. When a paraxial light beam illuminates obliquely on a slab, the local incident plane changes with the transverse wavevector κ_y: $\phi = \kappa_y / \sin\theta$, where ϕ is the azimuthal angle between the local incident plane and the x-axis. The local incident plane (azimuthal angle) increases linearly with κ_y. Before the transmission process, the incident field should be decomposed into the s and p waves, whose transmission coefficients are given in Fig. 2. According to Zhu et al. [18], the decomposed matrix under small incident angle approximation is given by

$$\tilde{U} = \begin{pmatrix} \cos\phi & \sin\phi \\ -\sin\phi & \cos\phi \end{pmatrix}. \quad (1)$$

The transmission matrix for s and p plane waves are

$$\tilde{F} = \begin{vmatrix} t_{pp} & t_{ps} \\ t_{sp} & t_{ss} \end{vmatrix}. \quad (2)$$

For the isotropic band, $|t_{ps}|$ and $|t_{sp}|$ are zero. For the anisotropic band, all the transmission coefficients vary with the azimuthal angle. Thus, the coefficients can be written into Taylor series with respective to incident θ and azimuthal ϕ angles. Under the first order approximation, we have

$$t_{ij} = t_{ij}(\theta, \phi) + \frac{k_x}{k_0} \frac{\partial t_{ij}(\theta, \phi)}{\partial \theta} + \frac{k_y}{k_0 \sin\theta} \frac{\partial t_{ij}(\theta, \phi)}{\partial \phi}. \quad (3)$$

The angular spectrum of the transmitted field is therefore $\tilde{\mathbf{E}}_t = \hat{U}^+ \hat{F} \hat{U} \tilde{\mathbf{E}}_i$. Here, we consider a simple case with a vertically-polarized one-dimensional (1D) Gaussian beam incident along the x-axis, $\tilde{\mathbf{E}}_i = \exp[-k_y^2 w_0^2/4]\hat{\mathbf{e}}_y$, with w_0 being the beam waist. The transmitted beam thus can be calculated as:

$$\tilde{\mathbf{E}}_t = \{(t'_{ps} - t'_{sp})\phi$$
$$\mp i(t_{pp} + t_{ss}) + [(t'_{ps} + t'_{sp})\phi \mp i(t_{ss} - t_{pp})]$$
$$\times \exp(\mp 2i\phi)\} \exp[-k_y^2 w_0^2/4]\hat{\mathbf{e}}_\pm. \quad (4)$$

$t'_{ij} = \partial t_{ij}(\theta, \phi)/\partial \phi$. The phases $\mp 2i\phi$ are the wave-vector-varying PB phases. The spin-dependent displacements are defined as $\Delta_\pm = \langle \tilde{E}_\pm | i\partial/\partial_{k_y} \tilde{E}_\pm \rangle / \langle \tilde{E}_\pm | \tilde{E}_\pm \rangle$, which are

$$\Delta_\pm = \pm \frac{\lambda}{\pi \sin\theta} \frac{\text{Re}[t_{ss}^*(t_{pp} - t_{ss} - t'_{ps})]}{|t_{ss}|^2 + |t_{pp} - t_{ss} - t'_{ps}|^2/k_0^2 w_0^2}. \quad (5)$$

One can find from (5) that the spin-displacements origin from two parts: one is from the wave-vector-varying PB phases and the other from the azimuthal-dependent polarization conversion effect. It is worth to point out that the spin-dependent displacements are zero for tiny small incident angles, when a paraxial beam transmitting through a uniaxial slab with its optical axis within the input interface. It is because the spin-displacements induced by the wave-vector-varying PB phases and azimuthal-dependent cross polarization conversion effect are canceled out. Moreover, based on Bloch modes that rely on only symmetry and periodicity, our proposal for spin separation is substrate independent [27], [29], [31], [32].
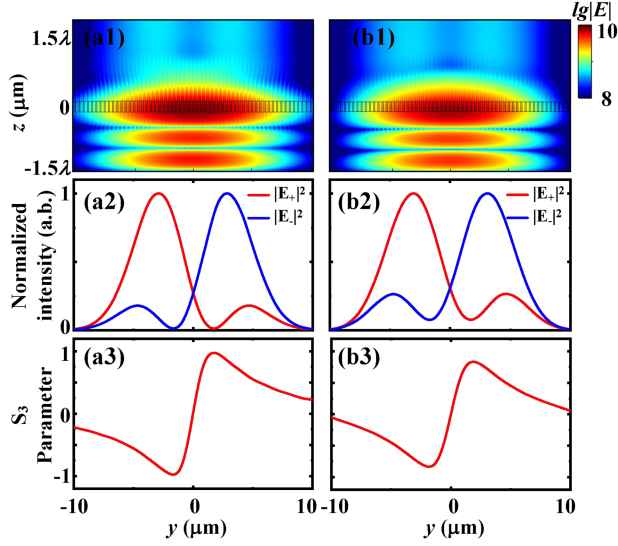
Fig. 3. (a1), (b1) Simulated intensity distributions in the yz plane for obliquely incident 1D beams. (a2), (b2) Normalized intensity profiles of RCP and LCP components of the transmitted beam at the output interface. (a3), (b3) Stokes parameters S_3 of the transmitted beam at the output interface. The dark lines highlight the PhC slab. In the simulations, the wavelength and incident angle $(\lambda, \theta) = (493 \text{ nm}, 2°)$ (a1)–(a3) and $(542 \text{ nm}, 4°)$ (b1)–(b3).

III. SIMULATION

To verify the PSHE in PhC slabs, we perform 3D numerical simulations with the finite element method (COMSOL Multiphysics 5.6). Here, the incident interface is selected as the xz plane, and the angle between the incident direction and z-axis is θ as shown in Fig. 1(a). For simplicity, 1D Gaussian beams are employed in the simulation, thus the period boundary condition can be used in the x-direction. To save the simulation time, the beam waists of the incident beams are set as 5 μm, and the simulation region is $a \times 150a \times (3\lambda + 5t)$. For the s-polarized incident beams, the simulated intensity distributions in the yz plane are given in Fig. 3(a1), (b1) for the the wavelength and incident angle (λ, θ) being (493 nm, 2°) (a1) and (542 nm, 4°) (b1), respectively. The peak intensities are found in within the PhC slab owing the local confinement effect of light fields. The RCP and LCP components of the transmitted light field will be moved toward opposite direction.

The transmitted light field are monitored at the $z = (3\lambda+5t)/2$ plane, where the local confinement effect can be neglected (see Fig. 3(a1), (b1)), thus the separation of the RCP and LCP components can be well observed. As shown in Fig. 3(a2), (b2), the intensity profiles of the RCP and LCP components are moved along the $\mp y$ directions for the both cases. The movements of the RCP and LCP components of the transmitted light fields are also evident in the Stocks parameter S_3, as shown in Fig. 3(a3), (b3). The positive and negative values of S_3 are separated by the $y = 0$ line, indicating that the transmitted light fields are in opposite handness polarization states for the $\pm y$ regions.

Fig. 4(a) gives the Spin-dependent displacements as functions of the incident angle for the operation wavelength of 493 nm, where the solid and dotted lines denote the theoretical and simulated results. The theoretical solid lines are calculated according to (5). The theoretical and simulated results are in
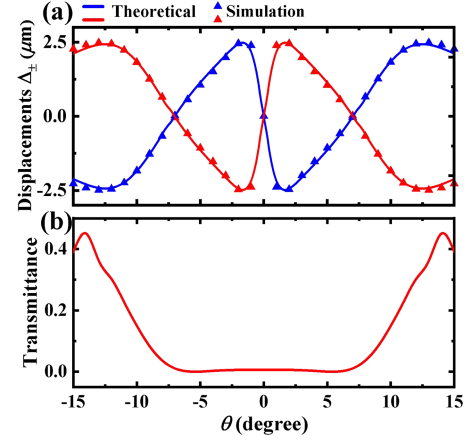

Fig. 4. Spin-dependent displacements (a), Transmittance (b) as functions of the incident angle for the operation wavelength of 493 nm. In (a), the solid and dotted lines denote the theoretical and simulated results.
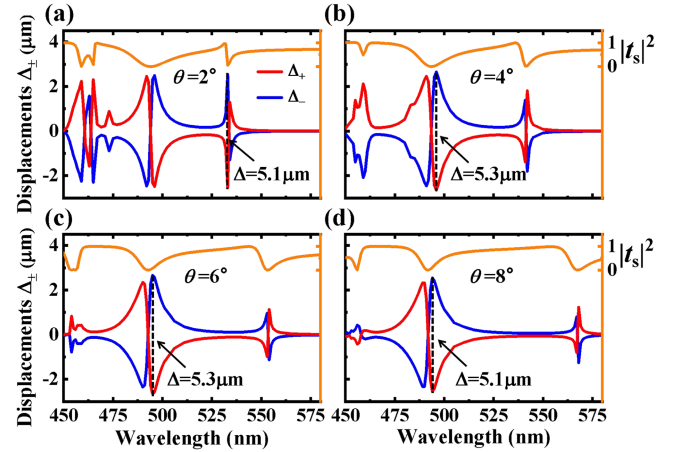

Fig. 5. Spin-displacements and transmittance $|t_s|^2$ as functions of the wavelength for different incident angles.

good agreement. The small disagreements are mainly due to the small beam waist (5 μm), which cannot ensure the paraxial approximation. For case of $\lambda = 493$ nm, the spin-displacements reach peak values at $\theta = \pm 2°$ and $\pm 12°$. At $\theta = \pm 2°$, the spin separation $\Delta = |\Delta_+ - \Delta_-| = 5$ μm, identical to the incident beam waist. Fig. 4(b) shows the transmittances of light beams. The peaks of the spin-displacements are usually accompanied with the low transmittances, lower than 0.01. At the peaks of $\theta = \pm 12°$ for $\lambda = 493$ nm, the transmittances are up to 0.3.

Fig. 5 shows the spin-displacements and transmittance $|t_s|^2$ as functions of the wavelength for the incident angles $\theta = 2°$, 4°, 6°, and 8°, respectively. From the transmittance, three dips can be noticed around the wavelengths of 460, 495 and 550 nm, among which the dip near 495 nm hardly changes with the incident angle, while the other two dips show a great dependence on the incident angle. The dip of transmittance at short wavelength (460 nm) moves to shorter wavelengths as the incident angle increases, while the dip at long wavelength (550 nm) behaves conversely.

Near the 460 nm, there are two close dips in the transmittance when $\theta = 2°$. These two dips merge gradually when the incident angle increase, and only one single dip can be
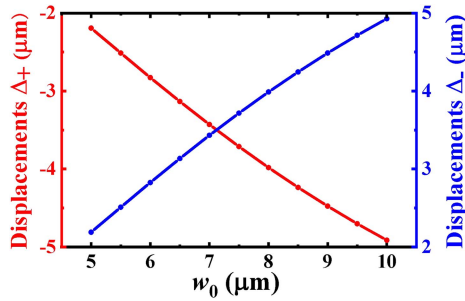
Fig. 6. Spin-displacements as a function of the beam waist w_0 for the operation wavelength and incident angle being 493 nm and $\theta = 2°$, respectively.

found when $\theta = 8°$. According to (5) the spin-displacements can be enhanced near the dips of $|t_{ss}|$ for y-polarized incident 1D Gaussian beams. At exactly the dip positions, however, no spin-dependent displacement occurs (see Fig. 5). Near the dip positions, the spin-displacements are very sensitive to the wavelength. The spin-displacements change their signs when the operation wavelength crosses the the dip of $|t_s|^2$, except for the wide dips near 460 nm when $\theta = 4°, 6°$. More noteworthy is that the spin-displacements around the wavelength of 495 nm exceed w_0 (5 μm), reaching 5.3 μm for the incident angles $\theta = 4°$ and $6°$. And for the incident angle $\theta = 2°$ and $8°$, the spin-displacements around the wavelengths of 535 nm and 495 nm are also larger than w_0, reaching 5.1 μm.

The dependence of the spin-dependent displacements on the incident beam waist is investigated. As shown in Fig. 6, the spin separation Δ increases from 5 to 10 μm, when the incident beam waist increase from 5 to 10 μm. It is worth to note that, for each incident beam waist, the spin separation can approach close to the beam wait by optimizing the incident angle and operation wavelength.

IV. CONCLUSION

In conclusion, a giant PSHE is demonstrated in a subwavelength-thickness PhC slab with a square lattice of air holes. The C_{4v} symmetry of the slab enables it to support both isotropic and anisotropic band structures. With the anisotropic band structures, the spin-displacements caused by the wave-vector-varying PB phases and azimuthal-dependent cross po-larization conversion effect. Both the theoretical prediction and numerical simulation results show that giant spin separations larger than the incident beam waist can be obtained. The spin separation can be adjusted in a wide range via changing the incident angle, wavelength and even the beam waist. These findings deepen the understanding of the PSHE and offer a flexible way for designing nanoscale spin-photonic devices.

REFERENCES

[1] O. Hosten and P. Kwiat, "Observation of the spin Hall effect of light via weak measurements," *Science*, vol. 319, no. 5864, pp. 787–790, 2008.

[2] M. Onoda, S. Murakami, and N. Nagaosa, "Hall effect of light," *Phys. Rev. Lett.*, vol. 93, no. 8, 2004, Art. no. 083901.

[3] X. Yin et al., "Photonic spin Hall effect at metasurfaces," *Science*, vol. 339, no. 6126, pp. 1405–1407, 2013.

[4] W. Long et al., "Optimized weak measurement of orbital angular momentum-induced beam shifts in optical reflection," *Photon. Res.*, vol. 7, no. 11, pp. 1273–1278, 2019.

[5] H. Dai et al., "Direct visualizing the spin Hall effect of light via ultrahigh-order modes," *Phys. Rev. Lett.*, vol. 124, no. 5, 2020, Art. no. 053902.

[6] W. Zhu et al., "Tunable spin splitting of Laguerre–Gaussian beams in graphene metamaterials," *Photon. Res.*, vol. 5, no. 6, pp. 684–688, 2017.

[7] X. Zhou and X. Ling, "Enhanced photonic spin Hall effect due to sur-face plasmon resonance," *IEEE Photon. J.*, vol. 8, no. 1, Feb. 2016, Art. no. 4801108.

[8] W. Zhu et al., "Large spatial and angular spin splitting in a thin anisotropic ε-near-zero metamaterial," *Opt. Exp.*, vol. 25, no. 5, pp. 5196–5205, 2017.

[9] X. Zhou et al., "Identifying graphene layers via spin Hall effect of light," *Appl. Phys. Lett.*, vol. 101, no. 25, 2012, Art. no. 251602.

[10] T. Zhu et al., "Generalized spatial differentiation from the spin hall effect of light and its application in image processing of edge detection," *Phys. Rev. Appl.*, vol. 11, no. 3, 2019, Art. no. 034043.

[11] X. Zhou, L. Sheng, and X. Ling, "Photonic spin Hall effect enabled refractive index sensor using weak measurements," *Sci. Rep.*, vol. 8, no. 1, pp. 1–8, 2018.

[12] P. Dong et al., "Controlling photonic spin Hall effect in graphene-dielectric structure by optical pumping," *New J. Phys.*, vol. 22, no. 11, 2020, Art. no. 113007.

[13] O. Takayama, J. Sukham, R. Malureanu, A. V. Lavrinenko, and G. Puentes, "Photonic spin Hall effect in hyperbolic metamaterials at visible wave-lengths," *Opt. Lett.*, vol. 43, no. 19, pp. 4602–4605, 2018.

[14] X.-J. Tan and X.-S. Zhu, "Enhancing photonic spin Hall effect via long-range surface plasmon resonance," *Opt. Lett.*, vol. 41, no. 11, pp. 2478–2481, 2016.

[15] X. Zhou et al., "Controlling photonic spin Hall effect via exceptional points," *Phys. Rev. B*, vol. 100, no. 11, 2019, Art. no. 115429.

[16] Y.-Y. Fu et al., "Photonic spin Hall effect in PT symmetric metamaterials," *Front. Phys.*, vol. 14, no. 6, pp. 1–7, 2019.

[17] W. Zhu and W. She, "Enhanced spin Hall effect of transmitted light through a thin epsilon-near-zero slab," *Opt. Lett.*, vol. 40, no. 13, pp. 2961–2964, 2015.

[18] W. Zhu et al., "Wave-vector-varying Pancharatnam-Berry phase photonic spin Hall effect," *Phys. Rev. Lett.*, vol. 126, no. 8, 2021, Art. no. 083901.

[19] H. Chen et al., "High-performance photonic spin Hall effect in anisotropic epsilon-near-zero metamaterials," *Opt. Lett.*, vol. 46, no. 17, pp. 4092–4095, 2021.

[20] D. Dai, Z. Wang, and J. E. Bowers, "Considerations for the design of asymmetrical Mach–Zehnder interferometers used as polarization beam splitters on a submicrometer silicon-on-insulator platform," *J. Lightw. Technol.*, vol. 29, no. 12, pp. 1808–1817, Jun. 2011.

[21] K. Morita and H. Uenohara, "Analytical and experimental investigation of a silicon photonic two-stage Mach–Zehnder delay interferometer-type polarization beam splitter," *IEEE Photon. J.*, vol. 10, no. 3, Jun. 2018, Art. no. 6600908.

[22] C. R. Doerr et al., "Monolithic polarization and phase diversity coherent receiver in silicon," *J. Lightw. Technol.*, vol. 28, no. 4, pp. 520–525, Feb. 2010.

[23] C. F. R. Mateus, M. C. Y. Huang, L. Chen, C. J. Chang-Hasnain, and Y. Suzuki, "Broad-band mirror (1.12-1.62 μm) using a subwavelength grating," *IEEE Photon. Technol. Lett.*, vol. 16, no. 7, pp. 1676–1678, Jul. 2004.

[24] L. Xu et al., "Compact broadband polarization beam splitter based on multimode interference coupler with internal photonic crystal for the SOI platform," *J. Lightw. Technol.*, vol. 37, no. 4, pp. 1231–1240, 2019.

[25] Y. Ding and R. Magnusson, "Resonant leaky-mode spectral-band engineer-ing and device applications," *Opt. Exp.*, vol. 12, no. 23, pp. 5661–5674, 2004.

[26] S. Hernandez et al., "High performance bi-dimensional resonant grating filter at 850 nm under high oblique incidence of ~60°," *Appl. Phys. Lett.*, vol. 92, no. 13, 2008, Art. no. 131112.

[27] B. Wang et al., "Generating optical vortex beams by momentum-space polarization vortices centred at bound states in the continuum," *Nature Photon.*, vol. 14, no. 10, pp. 623–628, 2020.

[28] Y. Shen et al., "Structural colors from Fano resonances," *ACS Photon.*, vol. 2, no. 1, pp. 27–32, 2015.

[29] W. Liu et al., "Circularly polarized states spawning from bound states in the continuum," *Phys. Rev. Lett.*, vol. 123, no. 11, 2019, Art. no. 116104.

[30] C. Guo et al., "Photonic crystal slab Laplace operator for image differen-tiation," *Optica*, vol. 5, no. 3, pp. 251–256, 2018.

[31] J. Wang et al., "Shifting beams at normal incidence via controlling momentum-space geometric phases," *Nature Commun.*, vol. 12, no. 3, pp. 6046–6052, 2021.

[32] Z. F. Sadrieva et al., "Transition from optical bound states in the continuum to leaky resonances: Role of substrate and roughness," *ACS Photon.*, vol. 4, no. 4, pp. 723–727, 2017.